

# Image potential and field states at Ag(100) and Fe(110) surfaces

A. Hanuschkin, D. Wortmann, and S. Blügel

*Institut für Festkörperforschung, Forschungszentrum Jülich, D-52425 Jülich, Germany*

(Received 19 June 2007; revised manuscript received 6 August 2007; published 15 October 2007)

By combining the first-principles concept based on the density functional theory with a model vacuum potential, we calculate image potential states and analogous ones in the presence of an electric field applied on a nonmagnetic Ag(100) surface and a magnetic Fe(110) surface. Our investigations are based on the Green-function embedding technique, which allows us to treat a truly semi-infinite surface and whence yields a continuum of bulk states. This turns out to be of crucial importance in order to investigate the qualitative difference between localized image or field states located in a band gap of the substrate and states in resonance with bulk states present at the same energies. This difference leads to remarkable changes in the binding energy versus field dispersion of the states. Furthermore, we show that in the case of the Fe(110) surface, the calculated magnetic exchange splitting increases with the electric field and is also modified by the transition from field states to surface resonance states.

DOI: [10.1103/PhysRevB.76.165417](https://doi.org/10.1103/PhysRevB.76.165417)

PACS number(s): 73.20.-r, 71.15.Mb, 73.20.At, 68.37.Ef

## I. INTRODUCTION

For the understanding of the electronic properties of surfaces in particular and surface science in general, image potential states proved to play a prominent role. These states occur as a Rydberg-like series of surface states close to the vacuum level confined by the surface on the one side and the slowly  $1/z$ -like decaying image potential on the other side. Hence, image states are located relatively far away from the surface, have a long lifetime and, thus, can be ideally observed experimentally by modern methods like two-photon photoemission,<sup>1</sup> inverse photoemission,<sup>2</sup> and scanning tunneling microscopy<sup>3,4</sup> (STM). These states and the corresponding experimental results are also easily described by rather simple theoretical models, making them ideal spectator states to probe the surface and the electronic structure.<sup>5-9</sup> The binding energies can be expressed<sup>8</sup> by a series of image potential (or Rydberg) states labeled by an index  $n$  and measured from the vacuum level  $E_{\text{vac}}$ ,

$$E_n = E_{\text{vac}} - \frac{13.6}{[4(n+a)]^2}, \quad n = 1, 2, 3, \dots, \quad (1)$$

in units of eV, where the quantum defect  $a$  has to be introduced due to the finite tail of the wave function overlapping with the crystal. Recently, increasing effort is made to extract details of the electronic structure of the surface from such measurements. For example, the investigation of the exchange splitting of the image states became feasible.<sup>10</sup>

Using the spectroscopy mode of a spin-polarized STM, the magnetic splitting of the image states can be investigated locally and, hence, the underlying magnetic structure can be resolved.<sup>11</sup> In these experiments, a rather large bias voltage is applied between the STM tip and the sample surface such that electrons can tunnel into the image states. Strictly speaking, the states observed are no longer simple image states as the applied bias leads to a substantial electric field applied to the surface. Hence, the electrons are no longer confined by a  $1/z$ -like potential but experience the additional linear potential of the field. Following Binnig *et al.*,<sup>3</sup> we will use the term “field states” for these generalized image states. An

alternative view on these states is their description as resonances in the field emission of the tip. This picture enables the description of their intrinsic lifetime and is useful for the interpretation of the peak shape observed in the STM experiments.<sup>12,13</sup> However, it is difficult to include both the surface and the tip effects, which would require a nonequilibrium treatment of the full junction. In the spirit of the STM as a tool to investigate surface properties, we will neglect these tip interaction effects.

To provide some insight into the subtle changes of the image and field states from the simple rule expressed by Eq. (1) due to the electronic structure of the surface, we perform first-principles density functional theory (DFT) calculations. Two systems are presented, the Ag(100) surface and the Fe(110) surface. We use the simpler, nonmagnetic Ag surface to introduce the general effects expected in the transition from image states to field states and to verify the method by comparing to experiments<sup>14-20</sup> and simple models,<sup>1</sup> while we focus on the exchange splitting of these states in the case of the ferromagnetic Fe surface.<sup>11,21-26</sup> Recently, both surfaces were investigated, in the case of Ag(100) by STM<sup>19,20</sup> and the Fe(110) surface by spin-polarized STM.<sup>11</sup> These experiments require a theoretical investigation of the field states, which we will present and discuss in Secs. III and IV, respectively.

## II. THEORY

Within the local density (LDA) and generalized gradient approximations (GGA) commonly used for the exchange correlation potential to the density functional theory, the calculation of image potential states is not possible. In particular, the only input into the LDA is the exponentially decaying local charge density in vacuum and, hence, the LDA yields a potential decaying exponentially toward the vacuum level. In order to fix this deficiency, we replace the LDA or GGA vacuum potential by a model potential with the correct  $1/z$  asymptotic tail. Following similar work by other groups<sup>5-9</sup> and adding a constant electric field  $\xi$ , we assume the following form of the potential in vacuum:

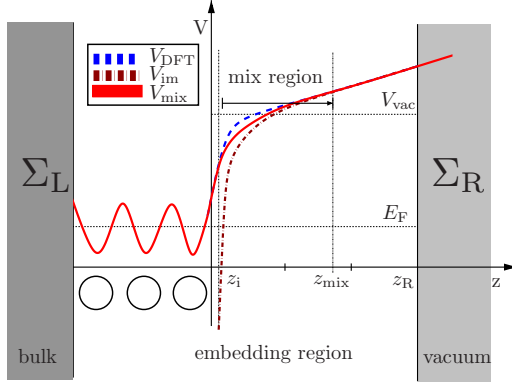


FIG. 1. (Color online) The embedding region is bound by the bulk on the left side and the vacuum region on the right side. At the boundary, the embedding potentials  $\Sigma_L$  and  $\Sigma_R$  set the correct boundary conditions in the KS Hamiltonian. The DFT potential (blue/dashed) is connected to the correct  $1/z$ -like-potential (brown/dashed dotted) in some mixing region into it until the correct behavior of the potential (red/solid) is modeled.

$$V_{\text{im}}(z) = V_{\text{vac}} - (13.6)(2) \frac{1}{4|z - z_i|} + z\xi, \quad (2)$$

in units of eV, where  $z$  is the coordinate normal to the surface,  $V_{\text{vac}}$  denotes the vacuum level of the potential, and  $z_i$ , the so-called image plane position, is a parameter. In our calculations, the vacuum level is taken from the solution of the Hartree potential, i.e., it is assumed to be the value in the vacuum region at which the Hartree potential becomes constant at a reasonable distance from the surface at zero field. The image plane position can also be calculated as the center of the static screening charge.<sup>7</sup> We determine the screening charge by calculating the difference of the lateral averaged charge with and without applied electric field. The center of the screening charge for  $\xi \rightarrow 0$  can be regarded as the image plane position. The image states are unoccupied. They can be investigated by STM if a positive electric field is applied, enabling the electrons to tunnel from the STM tip into the image potential states. Therefore, throughout the work, we use positive electric fields only. In order to ensure a continuous transition of the DFT potential to the model potential in vacuum, we adopt a simple mixing scheme in which we change the potential according to

$$V_{\text{mix}}(z) = V_{\text{DFT}}(z)f(z) + V_{\text{im}}(z)[1 - f(z)], \quad (3)$$

where  $f(z)$  changes from 1 to 0 as  $\cos(z)$  in a chosen mixing region up to  $z_{\text{mix}}$ . In Fig. 1, the resulting potential and the potential mixing are sketched.

Our simple ansatz for the potential will not be able to predict the experimentally observed image states in all details—e.g., it misses their finite lifetimes—but their basic properties can be reproduced. As the potential far in vacuum as well as the DFT potential deep in the bulk produce the correct electronic structure, only states localized in the surface region are expected to depend on the *ad hoc* ansatz of the mixed potential. Examples for such states are the lower image potential states and their strong dependence on the

model parameters like the image plane position, and details of the potential mixing indicate the deficiency of the model. The parameters of the model would allow the fitting of the image state energies to their experimental values. Instead, as our main aim is the investigation of the field dependence of the image states in the end, we used a rather minimal mixing region and fixed the image plane and the vacuum level as our findings will not depend on the exact details of these states. More sophisticated schemes<sup>27–29</sup> trying to yield a consistent treatment of the short range correlations as in our DFT potentials and the long range correlations leading to the  $1/z$  have been proposed and can be applied in a further step to shed light on these details.

Our actual DFT calculations are performed employing GGA in the Perdew-Burke-Ernzerhof<sup>30</sup> parametrization using the embedded Green-function method,<sup>31–34</sup> which has been recently implemented within the context of the full-potential linearized augmented plane-wave method by Wortmann *et al.*<sup>35,36</sup> as part of the FLEUR project.<sup>37</sup> In this method, the surface is modeled by a few atomic layers (the embedded region) which are embedded as a sandwich between semi-infinite bulk and vacuum. The usual Kohn-Sham (KS) Hamiltonian  $H_{\text{KS}}$  of the surface or embedding region is modified by two additional surface terms acting on the embedding surfaces toward the bulk (L) and the vacuum (R).<sup>31</sup> Thus, the Schrödinger equation in the embedding region can be written as

$$[H_{\text{KS}}(\vec{r}) - E]\phi(\vec{r}) + \frac{1}{2} \sum_{S=L,R} \delta(n - n_S)[\partial_n \phi(\vec{r}) - \partial_n \psi_S(\vec{r})] = 0, \quad (4)$$

with  $n$  denoting the coordinate normal to the embedding surfaces located at  $n_{L/R}$ ,  $\phi$  is the wave function inside the embedding region, and  $\psi_{L/R}$ , the wave function outside this region. Thus, the additional term in Eq. (4) is ensuring that the total wave function has no kink at the embedding surfaces. The outer wave functions can be substituted by introducing energy dependent operators, so-called embedding potentials  $\Sigma_{L/R}$ , leading to a modified Hamiltonian

$$H_{\text{emb}} = H_{\text{KS}} + \frac{1}{2} \sum_{S=L,R} \delta(n - n_S) \left( \frac{\partial}{\partial n} - 2\Sigma_S \right). \quad (5)$$

The key quantities of the method are the embedding potentials  $\Sigma_{L/R}$  controlling the boundary conditions at the embedding surfaces and, thus, ensuring that the Green function  $G(E)$  obtained from

$$[H_{\text{emb}}(E) - E]G(E) = 1 \quad (6)$$

is the Green function of the infinite surface. In our calculations, the left embedding potential  $\Sigma_L$  is obtained from a separate calculation of the bulk substrate,<sup>35</sup> while the right potential  $\Sigma_R$  contains the information about the decay of the Green function into vacuum. This can be calculated analytically for the case of a constant potential,<sup>33,34</sup> and can be obtained from a simple numerical integration in the case of the  $1/z$  potential,<sup>38</sup> and an additional applied field. The analytic image potential [Eq. (2)] is set up on a mesh and the

value of the wave function is calculated by solving the one-dimensional Schrödinger equation numerically by the Numerov algorithm, starting with an initial wave function of free electrons far in the vacuum. The embedding potential can be expressed by the wave function  $\psi$  and its surface normal derivative  $\partial_n \psi$  at the embedding plane<sup>31</sup>  $z_R$ :

$$\Sigma_R(E) = \frac{\partial_n \psi(z_R)}{2\psi(z_R)}. \quad (7)$$

The first derivative of  $\psi(z_R)$  is calculated by finite differences.

### III. IMAGE POTENTIAL STATES OF Ag(100)

To validate our method and to introduce the basic features of image and field states, we first investigate the Ag(100) surface. Our setup consists of an embedded region of five silver layers sandwiched between bulk silver and vacuum. The interlayer distances of the topmost three surface layers have been relaxed beforehand using a standard film calculation with the FLEUR code.<sup>37</sup> This yields relative changes of the interlayer spacing of  $\Delta_{12} = -1.2\%$ ,  $\Delta_{23} = +0.9\%$ , and  $\Delta_{34} = +0.9\%$  relative to the bulk lattice constant of  $a_0 = 7.84$  a.u. (4.15 Å) for the first, second, and third layers in good agreement with earlier publications<sup>39–41</sup> and the experimental lattice constant of 4.09 Å.<sup>42</sup> For this relaxed surface, we obtain a work function ( $\Phi = V_{\text{vac}} - E_F$ ) of 4.25 eV, which is slightly below the measured value of around 4.4 eV.<sup>15,18,43</sup>

By applying the embedding Green-function method, a slightly larger work function of 4.58 eV is obtained. In order to investigate the image potential states, we take the electrostatic image plane position given by Ishida and Liebsch<sup>44</sup> of 2.86 a.u. on the vacuum side of the surface relative to the atomic position of the topmost layer. This choice is also in good agreement with the image plane obtained from the center of the screening charge, which we determine to be at 2.7 a.u. In our calculation, the embedding plane is positioned at a distance of 16 a.u. measured from the position of the surface atoms. We use the GGA DFT potential everywhere except for the last 2 a.u. prior to the embedding plane, in which we mix the image potential and the DFT potential. Thus, only a small change in the potential is introduced.

Figure 2 shows the  $\vec{k}$ -resolved local density of states (LDOS) at  $\vec{k}_{\parallel} = \vec{\Gamma}$ . The first four image potential states ( $n = 1, \dots, 4$ ) are visible at  $-0.613$ ,  $-0.182$ ,  $-0.087$ , and  $-0.031$  eV. In principle, these states lead to a delta peak in the density of states, which is, however, artificially broadened by adding a small imaginary part of 2.7 meV to the energy. The dashed vertical lines indicate experimental results obtained by Schuppler *et al.*<sup>15</sup> by two-photon photoemission, and the solid line highlights the position of the vacuum level. The calculated image potential states have slightly higher binding energies than in this experiment, a discrepancy which can partly be assigned to the overestimation of the work function and could be fixed by adjusting the image plane and the potential mixing. With increasing order of the image state, the height of the peaks decreases as can be observed in Fig. 2. This is a direct result of the shift of the

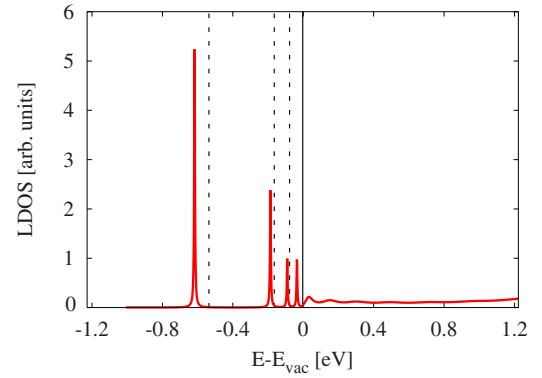


FIG. 2. (Color online) LDOS of the surface layer of a Ag(100) surface at  $\vec{k}_{\parallel} = \vec{\Gamma}$ . The energy is given relative to the vacuum level. Below the vacuum level, four delta peaks indicate the image potential energies. Above the vacuum energy, a free-electron-like LDOS is obtained. Experimental results from Schuppler *et al.* (Ref. 15) are indicated by dashed lines.

weight into vacuum for these states. By investigating the decay of the states into the Ag bulk, a perfect exponential decay with  $\kappa_{n=1} = 0.091$  a.u.<sup>-1</sup>,  $\kappa_{n=2} = 0.088$  a.u.<sup>-1</sup>,  $\kappa_{n=3} = 0.086$  a.u.<sup>-1</sup>, and  $\kappa_{n=4} = 0.086$  a.u.<sup>-1</sup> can be observed for the  $n = 1, 2, 3$ , and 4 image states, respectively. These values correspond to values obtained from the complex band structure<sup>45,46</sup> of the silver substrate shown in Fig. 3.

The parallel components of  $\vec{k}$  are chosen to be at the  $\vec{\Gamma}$  point of the two-dimensional Brillouin zone. The black lines represent the band structure of Bloch states with real  $\vec{k}$  vectors along a line in the bulk Brillouin zone which is projected onto the same  $\vec{k}_{\parallel}$  point of the two-dimensional Brillouin zone. The red lines represent states with  $k_z = q_z + i\kappa$ , where  $q_z$  is equal to 0. The green lines belong to  $q_z = \frac{2\pi}{a_0}$ . These evanescent states connect Bloch bands in a band gap by loops. We find the band gap to be 4.7 eV in total. The band edge is located at around 1.7 eV above the vacuum level. In this case, the  $\vec{k}$  vectors with the smallest imaginary values in the band gap are given by the green line connecting the band edges of the gap. Thus, the values of the exponential decay of the image states are determined by the values of this green line at the image state energies.

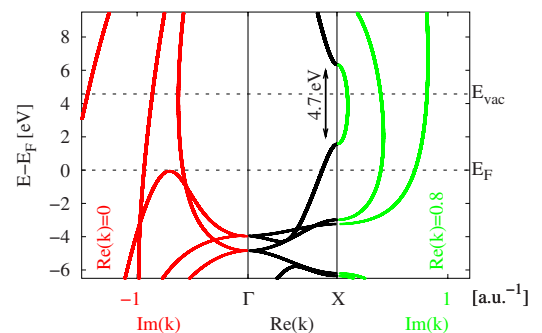


FIG. 3. (Color online) Complex band structure of Ag. Black lines represent the Bloch band between  $\Gamma$  and X. Red lines belong to complex bands with  $\text{Re}(\vec{k}) = 0$  and green lines to complex bands with  $\text{Re}(\vec{k}) = \frac{2\pi}{a_0}$ .  $a_0$  denotes the lattice constant of silver.

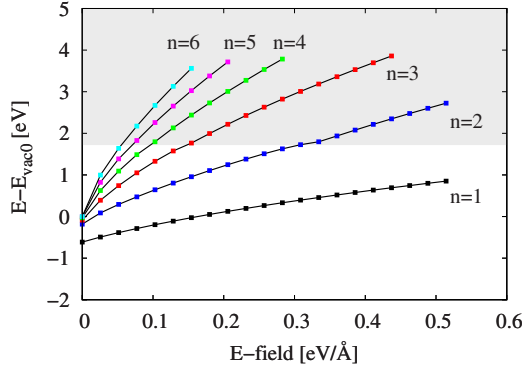


FIG. 4. (Color online) Field states of Ag(100) at  $\vec{k}_{\parallel}=\vec{\Gamma}$ . At around 1.7 eV, a change in slope can be seen. At this point, the upper band edge of the substrate is reached and the field states become resonance states. The projected band of the silver substrate is indicated by the shaded region.

By applying a positive electric field to the surface, the image potential states turn into field states. The electric field applied pushes the electron back into the Ag substrate and, thus, it is expected to have a particularly strong effect on the higher image states, which have a considerable weight in vacuum. Even for small fields, the energy for the Rydberg states  $n \rightarrow \infty$  is no longer the vacuum energy.

In Fig. 4, we show the energies of the image and/or field states as function of the electric field. The peak positions of Fig. 2 can be found to be the data points at zero field strength. We find that with increasing electric field, the energy of the field states indeed rises. The qualitative behavior of the calculated field states is in accordance with experimental results<sup>3</sup> and reproduces the  $E \propto \xi^{2/3}$  result found for an infinite triangular potential well model.<sup>47</sup> While most of Fig. 4 might have been deduced from a much simpler calculation, a detail in this plot shows the advantage of our semi-infinite *ab initio* calculation. At approximately 1.7 eV above the vacuum level, the projected bulk band is reached and, hence, the field states are no longer localized at the surface but hybridize with states of the Ag substrate to form surface resonance states. This leads to a change in their field dependence, which manifests itself in the change in slope seen in the shaded area of Fig. 4.

#### IV. IMAGE POTENTIAL STATES OF Fe(110)

To model the Fe(110) surface, we use an embedding volume comprised of the topmost four layers. As the surface relaxations for this surface are small<sup>48–51</sup> and test calculations showed no substantial difference of our results between the relaxed surface and the one with atoms located at bulk truncated positions, we use here the unrelaxed, simple bulk terminated setup. A work function of 5.49 eV for the LDA<sup>52</sup> and 4.67 eV for the GGA is obtained for the unrelaxed embedding calculation with the experimental lattice constant of 2.87 Å.<sup>42</sup> The resulting work function is comparable to other *ab initio* calculations.<sup>24,48,53–55</sup> Measured values of the work function of Fe(110) are reported to be 5.12 eV (Ref. 21) and

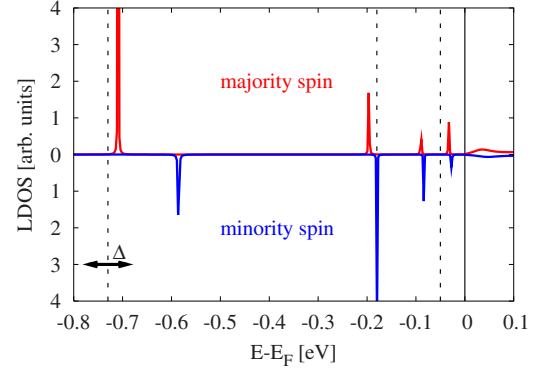


FIG. 5. (Color online) Spin-resolved LDOS of Fe(110) at  $\vec{k}_{\parallel}=\vec{\Gamma}$ . Dashed lines indicate experimental values by Fischer *et al.* (Ref. 21) of the spin averaged image state energies. They determined the upper limit for the magnetic splitting of the  $n=1$  state to 80 meV (marked by  $\Delta$ ). All energies are given relative to the vacuum energy marked by the black line.

5.05 eV,<sup>56</sup> very much in between our values. In order to estimate the image plane position, we calculate the center of the screening charge and obtain an image plane position of around 3.1 a.u. The  $n > 2$  states are insensitive to the position of the image plane, and an image plane position of 3.8 a.u. is used in the following because it leads to a good fit to the experimental energy of the first image state. The DFT potential is mixed with the image potential starting at 7.2 a.u. from the surface up to a distance of 8.38 a.u.

In Fig. 5, the spin-resolved LDOS is given at  $\vec{k}_{\parallel}=\vec{\Gamma}$  for the unrelaxed setup in the GGA. The energies of the image states are close to the measured energies by Fischer *et al.*,<sup>21</sup> indicated by dashed lines, and Himpel.<sup>22</sup> Different from the Ag(100) calculation, the two spins are no longer degenerated and an exchange splitting of the states can be observed. This splitting is most pronounced for the  $n=1$  state and decays rapidly for the higher Rydberg states. For the first Rydberg state ( $n=1$ ), we obtain a spin splitting of 133 meV, which is nearly twice as large as the splitting observed in experiment<sup>21,57</sup> or by theoretical approaches,<sup>22,24</sup> but within the range given by Borstel and Thorner<sup>2</sup> and close to  $85 \pm 20$  meV measured by Thomann *et al.*<sup>58</sup> The calculated splitting is nearly unaffected by variations of the image plane position and applied mixing region. Furthermore, by using different approximations for the exchange correlation potential, the magnitude of the splitting does not change significantly.

Figure 6 shows the evolution of the exchange-split image potential states with applied electric field. Most features seen in the upper panel correspond to the general trend seen in Fig. 4 for the Ag surface. The lower panel of Fig. 6 additionally shows the exchange splitting, i.e., the difference of the majority and minority curves of the upper panel. This plot shows rather drastic changes of the exchange splitting with respect to the applied field. For zero field, the splitting is very small for all states except for the  $n=1$  state. Indeed, it was shown that the splitting is expected<sup>24</sup> to decay with  $1/n^3$ , which can be roughly confirmed. This can be understood from the fact that the higher Rydberg states have their

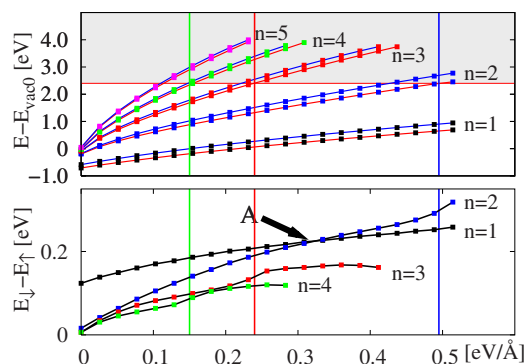


FIG. 6. (Color online) In the upper panel, the field states of Fe(110) at  $\vec{k}_{\parallel}=\vec{\Gamma}$  are shown. The difference between the majority state and the minority state is plotted in the lower panel. The slope of this magnetic exchange splitting changes. These positions are mapped onto the field state plot by the vertical lines, with colors corresponding to the number of the Rydberg state. It can be seen that they all cross the field state curve at the same energy of around 2.4 eV. This is indicated by the black horizontal line. The projected band of the majority spin starts at around 2.4 eV. It explains the features seen in the magnetic exchange splitting plot.

main weight in vacuum, where the potential is spin degenerate and only the lowest states have a significant overlap with the bulk potential. However, this picture changes for larger field. The states are pushed toward the surface and the exchange splitting strongly increases. Two further interesting features are remarkable in Fig. 6. At mark A the magnetic exchange splitting of the  $n=2$  state becomes larger than the splitting of the  $n=1$  state. Such an interesting crossover seems to be also present in experiment<sup>59</sup> and might be worth investigating with a refined model as the exact energy dispersion of the  $n=1$  state might be sensitive to our model parameters. Furthermore, the curves for the  $n > 1$  states exhibit a change in slope. The positions of the changes are marked (vertical lines) for the  $n=2, 3$ , and 4 states and pro-

jected into the plot of the Fe(110) field states. They all appear at the same energy (horizontal line) of  $\sim 2.4$  eV. At this energy, the majority band gap of the Fe(110) substrate ends. Hence, it can be concluded that the change in slope is a consequence of the field state approaching the continuum of Fe majority states and turning into a resonance. Before that, they are deflected, giving rise to bigger spin splitting. The minority spin states only interact with the corresponding states at  $\sim 3.9$  eV above the vacuum energy.

## V. CONCLUSIONS

In this paper, we investigated image states and field states using the truly semi-infinite surface provided by the Green-function embedding method. Our DFT calculations confirm the general trend found in simple one-dimensional models, but additionally indicate that these states also show features of the electronic structure of the surface and the substrate. In particular, the exchange splitting of the image and field states reflects the spin polarization of the surface potential. The transition from image and field states from being localized between the vacuum potential and a gap in the band structure of the substrate into a resonance state hybridizing with substrate states at energies not in a projected band gap can also lead to experimentally accessible changes in the energy versus field dispersion. These effects might be the origin of the experimentally observed field dependence of the exchange splitting in scanning tunneling spectroscopy. With this we would like to encourage further experimental work resolving the exchange splitting of image potential states and their field dependence.

## ACKNOWLEDGMENTS

We would like to thank A. Kubetzka for inspiring this work and for providing experimental input, and H. Ishida for his help in implementing the vacuum embedding potential.

- <sup>1</sup>T. Fauster and W. Steinmann, *Photonic Probes of Surfaces* (Elsevier, Amsterdam, 1995), Chap. 8, pp. 347–411.
- <sup>2</sup>G. Borstel and G. Thorner, *Surf. Sci. Rep.* **8**, 1 (1987).
- <sup>3</sup>G. Binnig, K. H. Frank, H. Fuchs, N. Garcia, B. Reihl, H. Rohrer, F. Salvan, and A. R. Williams, *Phys. Rev. Lett.* **55**, 991 (1985).
- <sup>4</sup>E. Louis, F. Flores, and P. M. Echenique, *Phys. Scr.* **37**, 359 (1988).
- <sup>5</sup>P. Cutler and J. Davis, *Surf. Sci.* **1**, 194 (1964).
- <sup>6</sup>J. A. Appelbaum and D. R. Hamann, *Phys. Rev. B* **6**, 1122 (1972).
- <sup>7</sup>N. D. Lang and W. Kohn, *Phys. Rev. B* **7**, 3541 (1973).
- <sup>8</sup>P. M. Echenique and J. B. Pendry, *J. Phys. C* **11**, 2065 (1978).
- <sup>9</sup>R. O. Jones, P. J. Jennings, and O. Jepsen, *Phys. Rev. B* **29**, 6474 (1984).
- <sup>10</sup>M. Donath, C. Math, M. Pickel, A. Schmidt, and M. Weinelt, *Surf. Sci.* (to be published).
- <sup>11</sup>A. Kubetzka, M. Bode, and R. Wiesendanger, *Appl. Phys. Lett.*

- 91**, 012508 (2007).
- <sup>12</sup>J. I. Pascual, C. Corriol, G. Ceballos, I. Aldazabal, H.-P. Rust, K. Horn, J. M. Pitarke, P. M. Echenique, and A. Arnau, *Phys. Rev. B* **75**, 165326 (2007).
- <sup>13</sup>S. Crampin, *Phys. Rev. Lett.* **95**, 046801 (2005).
- <sup>14</sup>A. Goldmann, V. Dose, and G. Borstel, *Phys. Rev. B* **32**, 1971 (1985).
- <sup>15</sup>S. Schuppler, N. Fischer, T. Fauster, and W. Steinmann, *Appl. Phys. A: Solids Surf.* **51**, 322 (1990).
- <sup>16</sup>W. Altmann, V. Dose, and A. Goldmann, *Z. Phys. B: Condens. Matter* **65**, 171 (1986).
- <sup>17</sup>B. Reihl, K. H. Frank, and R. R. Schlittler, *Phys. Rev. B* **30**, 7328 (1984).
- <sup>18</sup>B. Reihl and J. M. Nicholls, *Z. Phys. B: Condens. Matter* **67**, 221 (1987).
- <sup>19</sup>M. Pivetta, F. Patthey, M. Stengel, A. Baldereschi, and W. D. Schneider, *Phys. Rev. B* **72**, 115404 (2005).

- <sup>20</sup>H. C. Ploigt, C. Brun, M. Pivetta, F. Patthey, and W. D. Schneider (unpublished).
- <sup>21</sup>R. Fischer, N. Fischer, S. Schuppler, T. Fauster, and F. J. Himpsel, Phys. Rev. B **46**, 9691 (1992).
- <sup>22</sup>F. J. Himpsel, Phys. Rev. B **43**, 13394 (1991).
- <sup>23</sup>H. Scheidt, M. Glöbl, V. Dose, and J. Kirschner, Phys. Rev. Lett. **51**, 1688 (1983).
- <sup>24</sup>M. Nekovee, S. Crampin, and J. E. Inglesfield, Phys. Rev. Lett. **70**, 3099 (1993).
- <sup>25</sup>M. Nekovee and J. E. Inglesfield, Surf. Rev. Lett. **1**, 415 (1994).
- <sup>26</sup>M. Nekovee and J. Inglesfield, Prog. Surf. Sci. **50**, 149 (1995).
- <sup>27</sup>P. M. Echenique, J. Phys. C **18**, L1133 (1985).
- <sup>28</sup>P. De Andrés, F. Flores, P. M. Echenique, and R. H. Ritchie, Europhys. Lett. **3**, 101 (1987).
- <sup>29</sup>J. Jung, J. E. Alvarillos, E. Chacón, and P. García-González, J. Phys.: Condens. Matter **19**, 266008 (2007).
- <sup>30</sup>J. P. Perdew, K. Burke, and M. Ernzerhof, Phys. Rev. Lett. **77**, 3865 (1996).
- <sup>31</sup>J. Inglesfield, J. Phys. C **14**, 3795 (1981).
- <sup>32</sup>J. E. Inglesfield and G. A. Benesh, Phys. Rev. B **37**, 6682 (1988).
- <sup>33</sup>H. Ishida, Surf. Sci. **388**, 71 (1997).
- <sup>34</sup>H. Ishida, Phys. Rev. B **63**, 165409 (2001).
- <sup>35</sup>D. Wortmann, H. Ishida, and S. Blügel, Phys. Rev. B **65**, 165103 (2002).
- <sup>36</sup>D. Wortmann, H. Ishida, and S. Blügel, Phys. Rev. B **66**, 075113 (2002).
- <sup>37</sup><http://www.flapw.de>
- <sup>38</sup>G. Butti, S. Caravati, G. P. Brivio, M. I. Trioni, and H. Ishida, Phys. Rev. B **72**, 125402 (2005).
- <sup>39</sup>K. Bohnen, T. Rodach, and K.-M. Ho, *The Structure of Surfaces III* (Springer, New York, 1991).
- <sup>40</sup>S. Clarke, G. Bihlmayer, and S. Blügel, Phys. Rev. B **63**, 085416 (2001).
- <sup>41</sup>M. Methfessel, D. Hennig, and M. Scheffler, Phys. Rev. B **46**, 4816 (1992).
- <sup>42</sup>W. B. Pearson, *A Handbook of Lattice Spacings and Structures of Metals and Alloys* (Pergamon, London, 1958).
- <sup>43</sup>K. Giesen, F. Hage, F. J. Himpsel, H. J. Riess, and W. Steinmann, Phys. Rev. B **35**, 971 (1987).
- <sup>44</sup>H. Ishida and A. Liebsch, Phys. Rev. B **66**, 155413 (2002).
- <sup>45</sup>V. Heine, Proc. Phys. Soc. London **81**, 300 (1963).
- <sup>46</sup>V. Heine, Surf. Sci. **2**, 1 (1964).
- <sup>47</sup>A. J. Jason, Phys. Rev. **156**, 266 (1967).
- <sup>48</sup>P. Błoński and A. Kiejna, Surf. Sci. **601**, 123 (2007).
- <sup>49</sup>A. Stibor, G. Kresse, A. Eichler, and J. Hafner, Surf. Sci. **507-510**, 99 (2002).
- <sup>50</sup>M. J. S. Spencer, A. Hung, I. K. Snook, and I. Yarovsky, Surf. Sci. **513**, 389 (2002).
- <sup>51</sup>M. Eder, K. Terakura, and J. Hafner, Phys. Rev. B **64**, 115426 (2001).
- <sup>52</sup>U. V. Barth and L. Hedin, J. Phys. C **5**, 1629 (1972).
- <sup>53</sup>P. Błoński and A. Kiejna, Vacuum **74**, 179 (2004).
- <sup>54</sup>M. Aldén, S. Mirbt, H. L. Skriver, N. M. Rosengaard, and B. Johansson, Phys. Rev. B **46**, 6303 (1992).
- <sup>55</sup>H. L. Skriver and N. M. Rosengaard, Phys. Rev. B **46**, 7157 (1992).
- <sup>56</sup>G. Pirug, G. Broden, and H. P. Bonzel, Surf. Sci. **94**, 323 (1980).
- <sup>57</sup>F. Passek, M. Donath, K. Ertl, and V. Dose, Phys. Rev. Lett. **75**, 2746 (1995).
- <sup>58</sup>U. Thomann, C. Reuß, T. Fauster, F. Passek, and M. Donath, Phys. Rev. B **61**, 16163 (2000).
- <sup>59</sup>A. Kubetzka (private communication).